

Soft Matter

Accepted Manuscript



This is an *Accepted Manuscript*, which has been through the Royal Society of Chemistry peer review process and has been accepted for publication.

Accepted Manuscripts are published online shortly after acceptance, before technical editing, formatting and proof reading. Using this free service, authors can make their results available to the community, in citable form, before we publish the edited article. We will replace this *Accepted Manuscript* with the edited and formatted *Advance Article* as soon as it is available.

You can find more information about *Accepted Manuscripts* in the [Information for Authors](#).

Please note that technical editing may introduce minor changes to the text and/or graphics, which may alter content. The journal's standard [Terms & Conditions](#) and the [Ethical guidelines](#) still apply. In no event shall the Royal Society of Chemistry be held responsible for any errors or omissions in this *Accepted Manuscript* or any consequences arising from the use of any information it contains.

Construction of dissipative particle dynamics models for complex fluids via the Mori-Zwanzig formulation

Zhen Li,^a Xin Bian,^a Bruce Caswell^b and George Em Karniadakis^{a†}

Received Xth XXXXXXXXXXXX 20XX, Accepted Xth XXXXXXXXXXXX 20XX

We present a bottom-up coarse-graining procedure to construct mesoscopic force fields directly from microscopic dynamics. By grouping many bonded atoms in the molecular dynamics (MD) system into a single cluster, we compute both the conservative and non-conservative interactions between neighboring clusters. In particular, we perform MD simulations of polymer melts to provide microscopic trajectories for evaluating coarse-grained (CG) interactions. Subsequently, dissipative particle dynamics (DPD) is considered as the effective dynamics resulting from the Mori-Zwanzig (MZ) projection of the underlying atomistic dynamics. The forces between finite-size clusters have, in general, both radial and transverse components and hence we employ four different DPD models to account differently for such interactions. Quantitative comparisons between these DPD models indicate that the DPD models with MZ-guided force fields yield much better static and dynamics properties, which are consistent with the underlying MD system, compared to standard DPD with empirical formulae. When the rotational motion of the particle is properly taken into account, the entire velocity autocorrelation function of the MD system as well as the pair correlation function can be accurately reproduced by the MD-informed DPD model. Since this coarse-graining procedure is performed on an unconstrained MD system, our framework is general and can be used in other soft matter systems in which the clusters can be faithfully defined as CG particles.

1 Introduction

Atomistic simulation techniques such as molecular dynamics track the motion of individual atoms and allow precise reconstruction of the molecular structure and chemical/physical properties. However, in many applications of biological systems and soft matter physics, it is computationally impractical or impossible to produce large-scale effects with atomistic simulations¹ even though some simplifications such as the bead-spring models for polymers have been used². When only macroscopic properties are of practical interest, it may not be necessary to explicitly take into account all the details of material at the atomic scale. Coarse-grained (CG) approaches including Langevin dynamics and dissipative particle dynamics drastically simplify the atomistic dynamics by using a larger particle to represent a cluster of molecules^{3–5}. With less degrees of freedom, the CG model provides an economical simulation path to capture the observable properties of fluid systems on larger spatial and temporal scales beyond the capability of conventional atomistic simulations. With increasing attention on soft matter research, the CG modeling has become a rapidly expanding methodology especially in the fields of polymer and biomolecular simulation in recent years^{4,5}.

The basis for constructing CG models is the specification

^aDivision of Applied Mathematics, Brown University, Providence, RI 02912, USA

^bSchool of Engineering, Brown University, Providence, RI 02912, USA

†E-mail: george.karniadakis@brown.edu

of CG force fields governing the motion of the CG particles. Usually, empirical expressions for the CG potentials with adjustable coefficients are parameterized and optimized to generate desired properties. More complicated form for CG potentials can be optimized by relative entropy rate based methodology⁶ and Bayesian inference⁷, which may provide good approximation to the many-body potential of mean force. Typically, simulations using the optimized potentials produce correct results for equilibrium properties including pair correlation functions. However, the dynamical properties such as time correlations are difficult to be reproduced using these potentials. Furthermore, the empirical CG potentials obtained by numerical optimizations are in principle neither transferable to other systems, nor to the same system under different thermodynamic conditions⁸. This dramatically limits the convenience and generality of these optimized CG potentials.

Alternatively, with an elimination of fast variables by using Mori-Zwanzig (MZ) projection operators^{9,10}, the CG interactions can be directly evaluated from the microscopic dynamics by mapping the microscopic system to a CG/mesoscopic system. Based on the Mori-Zwanzig formalism, the fast degrees of freedom in the microscopic system are eliminated and their effects can be approximated by a stochastic dynamics under the effects of dissipative and fluctuating interactions. Several studies have been reported on the application of the Mori-Zwanzig projection operators, e.g., Akkermans and Briels¹¹ applied the projector operator formalism to develop a coarse-grained model of single polymer chain, and later Kinjo and

Hyodo¹² and Hijón et al.¹³ proposed the equations of motion for the dynamics of the mesoscopic variables with an explicit relationship to the microscopic description. Based on the Mori-Zwanzig formulation, the coarse-grained (mesoscopic) system can be described by the generalized Langevin equation¹⁴

$$\frac{d\mathbf{p}(t)}{dt} = - \int_0^t ds \frac{\gamma(t-s)\mathbf{p}(s)}{m} + \delta\mathbf{F}(t), \quad (1)$$

which is consistent with the framework of the dissipative particle dynamics (DPD)^{13,15}. Therefore, in the present work the DPD model is considered as the effective dynamics resulting from a projection of an underlying atomistic dynamics.

DPD was initially proposed by Hoogerbrugge and Koelman¹⁶ to combine the advantages of large timescale in lattice-gas automata and mesh-free algorithm in molecular dynamics (MD). Subsequently, the DPD modeling has been further developed and successfully used in simulations of complex systems including polymer solutions¹⁷, colloidal suspensions¹⁸, multiphase flows¹⁹ and biological systems²⁰. However, in these applications the parametrization of the DPD model is predominantly empirical. In fact, the DPD method has its roots in microscopic dynamics and it is usually considered as a coarse-grained MD model. Many different methods have been developed to incorporate the microscopic details into coarse-grained models to obtain an optimal conservative force. Examples include inverse Monte Carlo²¹, iterative Boltzmann inversion procedure²², force matching method²³, relative entropy framework²⁴, multi-scale coarse-graining method²⁵, and other approaches have been summarized by Noid²⁶. However, the conservative force itself cannot produce the correct dynamic properties. Generally speaking, the exclusion of the friction arising from fluctuating interactions will result in a faster CG dynamics than its underlying microscopic system²⁷. Therefore, the non-conservative interactions should be also included when transport dynamics is concerned.

To extract the non-conservative forces from the microscopic dynamics, constrained MD simulations have been performed to provide the necessary microscopic information. Akkermans and Briels¹¹ proposed an algorithm to calculate such interactions in a constrained MD simulation. Lei et al.¹⁵ and Hijón et al.¹³ also carried out constrained MD simulations to obtain the coarse-grained friction forces from the time-correlation function of the fluctuating force field of the MD system. Subsequently, Trément et al.²⁸ followed the framework proposed by Hijón et al.¹³ to calculate the coarse-grained forces from constrained MD trajectories and constructed DPD models of n-pentane and n-decane. However, the constraints imposed to MD system may alter the dynamics of the system. Lei et al.¹⁵ have reported that the equation of state and dynamic properties of a constrained MD system are highly dependent on the constraints.

In this paper, we will consider *unconstrained* MD systems of polymer melts to avoid the effects from artificial constraints. Our objective is to extract effective interactions governing DPD systems directly from the MD trajectories and reproduce the MD system (to a maximum degree) by using the DPD model. In practice, MD simulations consisting of Lennard-Jones (LJ) particles are performed. We coarsen the MD system by grouping many bonded LJ particles into single cluster to evaluate the conservative, dissipative and random forces governing the DPD system. The conservative force is determined by ensemble averaging the pairwise interactions between clusters, which is consistent with the force derived from the potential of the mean force. The non-conservative forces are computed based on the time-correlation function of the fluctuating force field in MD systems following the methodology used first by Lei et al.¹⁵ and subsequently Yoshimoto et al.²⁹ Since the total force between two neighboring clusters is generally not parallel to the radial direction, the coarse-grained force fields obtained from MD simulations contain both the radial and the perpendicular interactions. Moreover, the rotational motions of the finite-size clusters are explicitly observed. Here, four different DPD models are employed to utilize these mesoscopic information obtained from MD simulations. We demonstrate that the MD-informed DPD models have significantly better performance than conventional DPD in reproducing the underlying microscopic system.

The remainder of this paper is organized as follows: In section 2 we briefly introduce the theoretical background for mapping a microscopic system to a mesoscopic system based on the Mori-Zwanzig formulation. Section 3 describes in detail how to implement the coarse-graining procedure for construction of the mesoscopic force fields. Section 4 presents the quantitative comparisons between four DPD models and their performance in reproducing the MD system. Finally, we conclude with a brief summary and discussion in section 5.

2 Theoretical background

We consider an atomistically well-defined n -particle system whose microscopic state $\Gamma = \{\mathbf{r}^n, \mathbf{p}^n\}$ is identified with the coordinates \mathbf{r} and momenta \mathbf{p} of the atomic particles. The microscopic dynamics of the system is determined by the Hamiltonian,

$$H(\Gamma) = \sum_{i=1}^n \frac{\mathbf{p}_i^2}{2m_i} + \frac{1}{2} \sum_{i \neq j} V(\mathbf{r}_{ij}), \quad (2)$$

where $H(\Gamma)$ defines the phase space trajectories of the system $\Gamma \equiv \{\mathbf{r}_i, \mathbf{p}_i, i = 1, n\}$.

When the atomistic information is not of practical interest, the dynamics of the system can be represented by proper CG

variables such as the coordinate \mathbf{R} and translational momentum \mathbf{P} of the center-of-mass (COM) of a cluster of atoms, as well as the angular momentum \mathbf{L} when the rotational motion is considered,

$$\mathbf{R}_I = \frac{1}{M_I} \sum_{i=1}^{N_c} m_{Ii} \mathbf{r}_{Ii}, \quad (3)$$

$$\mathbf{P}_I = \sum_{i=1}^{N_c} \mathbf{p}_{Ii}, \quad (4)$$

$$\mathbf{L}_I = \sum_{i=1}^{N_c} (\mathbf{r}_{Ii} - \mathbf{R}_I) \times (\mathbf{p}_{Ii} - \mathbf{P}_I), \quad (5)$$

where N_c is the number of atomic particles in the I th cluster and $M_I = \sum_i m_{Ii}$ is the total mass. Each cluster consisting of N_c atomic particles is coarsened to be one CG particle in the coarse-graining procedure with a CG level of N_c . Here and in the following, the variables of CG particles are represented with capital symbols, such as M , \mathbf{R} , \mathbf{P} and \mathbf{L} represent mass, position, translational momentum and angular momentum, respectively, while the corresponding lowercases m , \mathbf{r} and \mathbf{p} denote the variables of atomic particles. Usually, the rotational momentum of a CG particle is neglected during coarse-graining. However, there is no evidence showing that the rotational momentum is dispensable for the finite-size CG particles. In the present study, we will examine rigorously this assumption.

We start with the projection formalism involving only translational momentum. The rotational momentum can be included by generalizing the momentum term in the equations. With the CG variables, the motion of the CG particles can be approximated via the Mori-Zwanzig projection^{11–13,15}

$$\begin{aligned} \frac{d}{dt} \mathbf{P}_I &= \frac{1}{\beta} \frac{\partial}{\partial \mathbf{R}_I} \ln \omega(\mathbf{R}) \\ &- \beta \sum_{J=1}^K \int_0^t ds \langle [\delta \mathbf{F}_I(t-s)][\delta \mathbf{F}_J(0)]^T \rangle \frac{\mathbf{P}_J(s)}{M_J} \\ &+ \delta \mathbf{F}_I(t), \end{aligned} \quad (6)$$

where $\beta = 1/k_B T$ with T the thermodynamic temperature and k_B the Boltzmann constant, $\mathbf{R} = \{\mathbf{R}_1, \mathbf{R}_2, \dots, \mathbf{R}_K\}$ is a phase point in the CG phase space, and $\omega(\mathbf{R})$ is defined as a normalized partition function of all the microscopic configurations at phase point \mathbf{R} given by

$$\omega(\mathbf{R}) = \frac{\int d^N \hat{\mathbf{r}} \delta(\hat{\mathbf{R}} - \mathbf{R}) e^{-\beta U}}{\int d^N \hat{\mathbf{r}} e^{-\beta U}}, \quad (7)$$

where U is the potential energy corresponding to the phase point \mathbf{R} , and the integrations are performed over all the possible microscopic configurations $\{\hat{\mathbf{r}}_i\}$.

In the right-hand side of Eq.(6), the first term represents the conservative force due to the change of microscopic configuration, and it is the ensemble average force on cluster I denoted as $\langle \mathbf{F}_I \rangle$. The last term of Eq. (6) $\delta \mathbf{F}_I$ is the fluctuating force on cluster I and it is given by $\delta \mathbf{F}_I = \mathbf{F}_I - \langle \mathbf{F}_I \rangle$ in which \mathbf{F}_I is the total force acting on the cluster I . The second term of Eq. (6) is the friction force determined by an integral of memory kernel of the fluctuating force.

The time scale of the fluctuating force $\delta \mathbf{F}_I$ is determined by the atomic collision time, while the characteristic time scale of the momentum is a relevant variable related to the mass of the particle. When the momentum of COM is slow variable due to the inertia of the CG particle while the fluctuating force is fast variable, the typical time scales of the momentum and the fluctuating force are separable and a Markovian process is expected. Then, the time correlation of the fluctuating force can be replaced by the Dirac delta function based on the Markovian approximation

$$\beta \langle [\delta \mathbf{F}_I(t-s)][\delta \mathbf{F}_J(0)]^T \rangle = 2\boldsymbol{\gamma}_{IJ} \delta(t-s), \quad (8)$$

$$\beta \int_0^t ds \langle [\delta \mathbf{F}_I(t-s)][\delta \mathbf{F}_J(0)]^T \rangle \frac{\mathbf{P}_J(s)}{M_J} = \boldsymbol{\gamma}_{IJ} \cdot \frac{\mathbf{P}_J(t)}{M_J}, \quad (9)$$

where the $\boldsymbol{\gamma}_{IJ}$ is the friction tensor defined by

$$\boldsymbol{\gamma}_{IJ} = \beta \int_0^\infty dt \langle [\delta \mathbf{F}_I(t)][\delta \mathbf{F}_J(0)]^T \rangle. \quad (10)$$

With the Markovian approximation given by Eqs. (8) and (9), the conservative, dissipative and fluctuating forces in Eq. (6) can be computed from the trajectories of atomistic simulations. Here, we assume that the non-bonded interactions between neighboring clusters in the microscopic system are explicitly pairwise decomposable³⁰, and hence the total force consists of pairwise forces, e.g. $\mathbf{F}_I \approx \sum_{J \neq I} \mathbf{F}_{IJ}$ and $\delta \mathbf{F}_I \approx \sum_{J \neq I} \delta \mathbf{F}_{IJ}$. However, when we consider the force \mathbf{F}_{IJ} that a molecule J exerts on another molecule I , in principle, \mathbf{F}_{IJ} involving multi-body effects depends on all the COM coordinates \mathbf{R} as well as their microscopic configurations. Although Eq. (6) based on the Mori-Zwanzig formalism is accurate, a direct computation of the multi-body interactions is very difficult, even for an one-dimensional harmonic chain³¹. In practice, we neglect the many-body correlations between different pairs, and assume that the force \mathbf{F}_{IJ} between two clusters I and J depends only on the relative COM positions \mathbf{R}_I and \mathbf{R}_J and is independent of the positions of the rest of clusters. It should be noted that this approximation is not just a pair approximation to the CG force field but is also an approximate decomposition into pairwise forces.

Based on the Markovian approximation and the neglect of many-body correlations, the fluctuating forces are independent for different pairs and uncorrelated in times^{15,29}, which leads to an approximation $\langle [\delta \mathbf{F}_I(t-s)][\delta \mathbf{F}_J(0)]^T \rangle \mathbf{V}_J(s) \approx \sum_{J \neq I} \langle [\delta \mathbf{F}_{IJ}(t-s)][\delta \mathbf{F}_{IJ}(0)]^T \rangle \mathbf{V}_{IJ}(s)$. This approximation

neglects correlations between different pairs and it will work less effectively when many-body correlations become important³². However, as we will show in section 4, this approximation yields good results in the cases of the present work. The details of calculating pairwise CG interactions from MD trajectories will be introduced in section 3.

3 Coarsening a microscopic system

To demonstrate the coarse-graining procedure, we consider a MD system consisting of many Lennard-Jones (LJ) particles. The effective interactions between CG particles are evaluated using the methodology described in section 2. In the present study, the molecule of a homostar, which is a kind of star polymer whose arms have the same chemical structure, are employed for the MD simulations. Each molecule of the star polymer is treated as a single CG particle during the coarse-graining process. In this section, we will show how a mesoscopic force field can be constructed directly from the trajectories of MD simulation rather than empirical expressions.

3.1 Microscopic model

MD simulations of star polymer melts are performed in a cubic computational box with periodic boundary conditions. Star polymers are represented as chains of beads connected by short springs^{33,34}. Each molecule of the star polymer has N_a arms with N_b monomers per arm. Excluded volume interactions between monomers are included via a purely repulsive Lennard-Jones potential also known as the Weeks-Chandler-Andersen (WCA) potential³⁵,

$$V_{WCA}(r) = \begin{cases} 4\varepsilon \left[\left(\frac{\sigma}{r}\right)^{12} - \left(\frac{\sigma}{r}\right)^6 + \frac{1}{4} \right], & r \leq 2^{1/6}\sigma \\ 0, & r > 2^{1/6}\sigma \end{cases} \quad (11)$$

where the cutoff distance $r_c = 2^{1/6}\sigma$ is chosen so that only the repulsive part of the Lennard-Jones potential is considered; also, ε sets the energy scale and σ the length scale of the monomers. Each arm of the star polymer is connected to a core atom, hence the total number of atoms per star polymer is $N_c = N_a \times N_b + 1$. For neighbouring monomers the bond interactions are modeled as a spring with a finitely extensible nonlinear elastic (FENE) potential³⁶,

$$V_B(r) = \begin{cases} -\frac{1}{2}kr_0^2 \ln [1 - (r/r_0)^2], & r \leq r_0 \\ \infty, & r > r_0 \end{cases} \quad (12)$$

where $k = 30\varepsilon/\sigma^2$ is the spring constant and $r_0 = 1.5\sigma$ determines the maximum length of the spring³³. Then, the total potential $V_{WCA}(r) + V_B(r)$ between connected monomers has a minimum at $r \approx 0.97\sigma$. The spring is made stiff and short enough to minimise neighbouring bonds from crossing each

other³⁴. However, we note that the use of infinitely extensible harmonic springs to model bond interactions¹³ is more likely to yield artificial bond crossings.

The combination of FENE and WCA potentials can successfully represent stretching, orientation, and deformation of polymer chains and simple biomolecules³⁶. This has been widely used for the investigation of viscoelastic behavior of polymer melts³⁷, stretching of polymers in flow³⁸, and other rheological properties³⁹. Though the strategy of coarse-graining is demonstrated with this model system, it is worth noting that the current scheme for atomistic-to-mesoscopic coarse-graining is not relevant to any specific system. The separation of lengthscales between microscopic and CG models will ensure that this scheme can work with truly atomistic models if it works on heuristic models with similar long-wavelength properties.

The polymer melts are modeled with 1000 molecules of star polymer in periodic cubic boxes of length $(1000N_c/\rho)^{1/3}$, in which ρ is the number density of monomers. The MD simulations are performed in a canonical ensemble (NVT) with the Nosé-Hoover thermostat^{40,41}. Throughout this paper, the results are interpreted with the reduced LJ units including length, mass, energy and time units being $\sigma = 1$, $m = 1$, $\varepsilon = 1$ and $\tau = \sigma(m/\varepsilon)^{1/2}$, respectively. The polymer volume fraction is $\psi = N(\pi/6)\sigma^3/Vol = \rho\pi/6$, where N is total number of monomers and Vol is the volume of the computational box. All the MD simulations are performed at the temperature $k_B T = 1.0$ with the integration time step $\delta t = 1.0 \times 10^{-3}\tau$.

Figure 1 displays the typical configurations of star polymers consisting of different number of monomers. When we evaluate the interactions between CG particles, the monomers in a given star polymer are grouped into a single cluster.

Prior to the calculation of the CG interactions between neighboring clusters, we need to equilibrate the polymer melts. For star polymer with short arms, the ideal way to generate

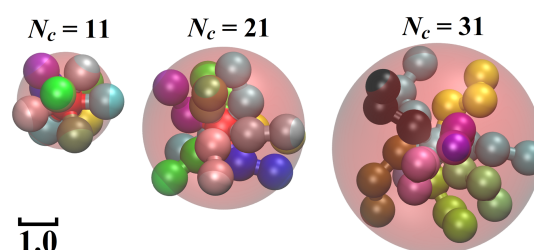


Fig. 1: Typical configurations of star-polymers consisting of different number of monomers. Star polymers have 10 arms with 1, 2 and 3 monomers per arm, hence $N_c = 11, 21$ and 31 , respectively. Monomers interact with WCA potential and connected monomers are attached by FENE bonds. One molecule of the star polymer is considered to be a CG particle when we evaluate the CG interactions.

an equilibrated melt is to start from an arbitrary initial configuration and continue the atomistic simulation out to several times the longest relaxation time of the polymer molecules³⁴. In this work, we constructed star polymer melts with random initial configurations and run the MD simulations for $10^3 \tau$ to obtain the thermal equilibrium state. Then, the rest of the computational time (up to $10^3 \tau$) is used to accumulate the interactions between clusters and construct the mesoscopic force fields for DPD models. Moreover, 1024 ensemble samples are used to minimise the uncertainties in our computations.

3.2 Analysis of the microscopic system

The properties of a polymer melt lie somewhere between liquids and solids depending on the concentration and microstructure of the polymers⁴². With the purpose of constructing a mesoscopic force field for DPD, which is designed for modeling fluids, the atomistic system of choice should be in the liquid state. Figure 2(a) presents the radial distribution functions (RDF) of the COM of star polymer $N_c = 11$ at different monomer densities $\rho = 0.4, 0.6$ and 0.8 . The curve of RDF exhibits sharp peaks as the monomer density increases, which indicates that the molecules of star polymer have less mobility and behave like crystal/solid at high monomer densities. However, at $\rho = 0.4$ the RDF shows absence of “long-range order” consistent with typical liquid-state RDFs. Therefore, $\rho = 0.4$ is adopted in our MD simulations, and the corresponding polymer volume fraction is $\psi = 0.209$.

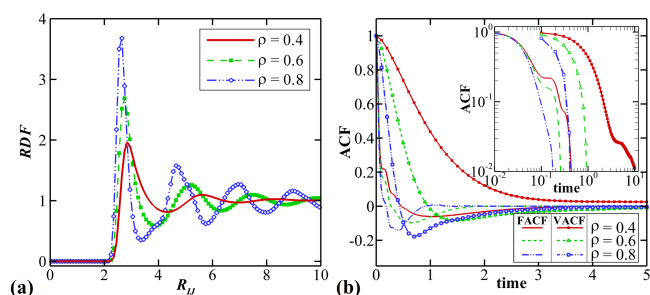


Fig. 2: (a) Radial distribution functions (RDF) of the center-of-mass (COM) of star polymers and (b) velocity and force autocorrelation functions of star polymers at different monomer densities $\rho = 0.4, 0.6$ and 0.8 , $N_c = 11$ and $k_B T = 1.0$. (Results from MD simulations.)

The velocity autocorrelation functions (VACF) and the force autocorrelation functions (FACF) of COM at various monomer densities are plotted in Fig. 2(b). For $\rho = 0.8$ the time scales of VACF and FACF are comparable and the Markovian approximation is questionable. By contrast, the VACF and the FACF at $\rho = 0.4$ have correlation times well-separated, hence a Markovian behaviour is expected. This further confirms that the monomer number density $\rho = 0.4$ is a

reasonable choice for the MD system to be coarse-grained.

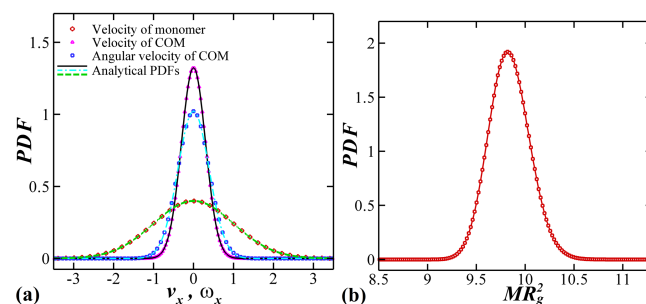


Fig. 3: (a) Verification of the equipartition theorem at the coarse-grained level with the PDFs of the translational and rotational motions about the COMs. Points correspond to MD results and lines are from analytical expressions. (b) Probability density function (PDF) of MR_g^2 of star polymers calculated by Eq. (15).

In a well-defined MD system consisting of N atoms, the temperature of the system is monitored with the average kinetic energy of its atoms given by $\langle \mathbf{p}^2/2m \rangle$. According to the equipartition theorem the thermal energy is shared equally among all of its degrees of freedom, and we have $\langle \mathbf{p}^2/2m \rangle = \frac{3}{2}k_B T$. If the atoms in the same molecule are packed into a cluster and we use the momentum \mathbf{P} and coordinate \mathbf{R} of the COM to describe the system, then the average kinetic energy of the COMs can be calculated as follows,

$$\begin{aligned} \left\langle \frac{\mathbf{P}_I^2}{2M_I} \right\rangle &= \frac{1}{K} \sum_I^K \left\langle \frac{\mathbf{P}_I^2}{2M_I} \right\rangle = \frac{1}{K} \sum_{I=1}^K \frac{1}{2M_I} \left\langle \left(\sum_{i=1}^{N_c} \mathbf{p}_{Ii} \right)^2 \right\rangle \\ &= \frac{1}{N} \sum_{I=1}^K \sum_{i=1}^{N_c} \left\langle \frac{\mathbf{p}_{Ii}^2}{2m} \right\rangle + \frac{1}{N} \sum_{I=1}^K \sum_{i \neq j}^{N_c} \frac{\langle \mathbf{p}_{Ii} \cdot \mathbf{p}_{Ij} \rangle}{2m}, \end{aligned} \quad (13)$$

where K is the number of clusters and $N_c = N/K$ is the number of atoms in each cluster. Here, all the atoms have the same mass m and we have $M_I = N_c \cdot m$. In the last equality of Eq.(13), the first term describes the average kinetic energy of atoms $\langle \mathbf{p}^2/2m \rangle$, and the second term is a summation of $\langle (\mathbf{p}_i \cdot \mathbf{p}_j)_{j \neq i} \rangle$ in the same cluster. When the thermal energy is distributed equally on all the degrees of freedom and $\langle \mathbf{P}^2/2M \rangle = \langle \mathbf{p}^2/2m \rangle$, the second term is expected to vanish. However, we need to explicitly check the validity of the equipartition theorem at the coarse-grained level. Figure 3(a) shows the probability density functions (PDFs) of the velocities of the monomer and the COM. For a particle-based system in thermal equilibrium, the PDF of velocity is given by

$$f(v_x) = \left(\frac{m}{2\pi k_B T} \right)^{1/2} \exp \left(-\frac{mv_x^2}{2k_B T} \right), \quad (14)$$

where m is the mass. The lines in Fig. 3 are analytical distributions while the symbols are obtained from the MD simulation.

It is obvious that the equipartition theorem is still valid for the quantities of COM. Thus, the CG systems should have the same thermal energy as its underlying microscopic systems.

To obtain the rotational inertia of the CG particles, we take the size of each cluster to be its gyration radius R_g defined by

$$M_I R_{gI}^2 = \sum_{i=1}^{N_c} m_{iI} \hat{\mathbf{r}}_{iI}^2 = \sum_{i=1}^{N_c} m_{iI} (\mathbf{r}_{iI} - \mathbf{R}_I)^2, \quad (15)$$

where M_I is the mass of cluster I , and $\hat{\mathbf{r}}_{iI} = \mathbf{r}_{iI} - \mathbf{R}_I$ are the relative displacements of particles i with respect to their COMs.

Figure 3(b) shows the PDF of MR_g^2 with the mean $\langle MR_g^2 \rangle = 9.83$ for the star polymer with $N_c = 11$. Considering the spherical symmetry of the star polymer, the rotational inertia of the CG particle is $I_{R_x} = \langle \sum m_i (\hat{y}_i^2 + \hat{z}_i^2) \rangle = \frac{2}{3} \langle MR_g^2 \rangle$. Thus, we found the rotational inertia $I_R = 6.55$ for the star polymer $N_c = 11$. With this I_R value, we also compare the PDF of the angular velocity about the COM with the analytical solution in the form of Eq. (14) with I_R instead of m , and find good consistency, as shown in Fig. 3(a).

3.3 Mesoscopic force field

Since the molecule of a star polymer consists of discrete monomers, the total force \mathbf{F}_{IJ} between two clusters I and J is generally not parallel to the radial vector \mathbf{e}_{IJ} , which is directed along center-to-center from J to I . Figure 4 displays a schematic picture depicting the three directions for considering pairwise interactions between clusters I and J . The symbol “||” in Fig. 4 represents the direction parallel to \mathbf{e}_{IJ} , while “ \perp_1 ” denotes the direction along the perpendicular velocity component $\mathbf{V}_{IJ}^{\perp_1} = \mathbf{V}_{IJ} - (\mathbf{V}_{IJ} \cdot \mathbf{e}_{IJ})\mathbf{e}_{IJ}$ and “ \perp_2 ” the direction orthogonal to both \mathbf{e}_{IJ} and \mathbf{V}_{IJ} .

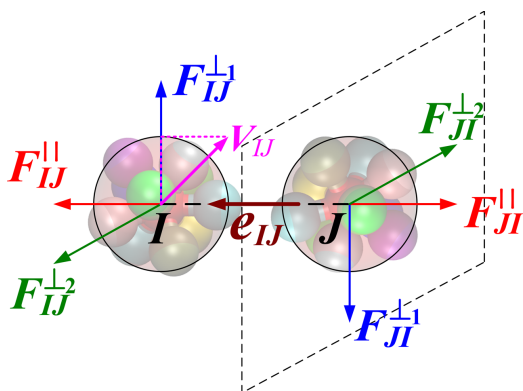


Fig. 4: Schematic depiction of the directions describing pairwise interactions between clusters I and J . The symbol “||” represents the direction parallel to \mathbf{e}_{IJ} , while “ \perp_1 ” denotes the direction along the perpendicular velocity component $\mathbf{V}_{IJ}^{\perp_1} = \mathbf{V}_{IJ} - (\mathbf{V}_{IJ} \cdot \mathbf{e}_{IJ})\mathbf{e}_{IJ}$, and “ \perp_2 ” the direction orthogonal to both \mathbf{e}_{IJ} and \mathbf{V}_{IJ} .

3.3.1 Conservative force. The rotational symmetry of the CG pairs about the \mathbf{e}_{IJ} axis suggests that, on average, \mathbf{F}_{IJ} has zero components in the \perp_1 and \perp_2 directions, which has been verified by computing the mean transversal forces $\langle \mathbf{F}_{IJ} \cdot \mathbf{e}_{IJ}^{\perp_1} \rangle$ and $\langle \mathbf{F}_{IJ} \cdot \mathbf{e}_{IJ}^{\perp_2} \rangle$ based on MD data. Hence, the average pairwise force $\langle \mathbf{F}_{IJ} \rangle$, which is taken as the conservative force \mathbf{F}_{IJ}^C , will be of the form,

$$\langle \mathbf{F}_{IJ} \rangle = \mathbf{F}_{IJ}^C = F_{IJ}^C(R_{IJ})\mathbf{e}_{IJ} = \alpha \cdot \omega_C(R_{IJ})\mathbf{e}_{IJ}, \quad (16)$$

where \mathbf{e}_{IJ} is the unit vector from particle J to I given by $\mathbf{e}_{IJ} = (\mathbf{R}_I - \mathbf{R}_J)/R_{IJ}$ with $R_{IJ} = |\mathbf{R}_I - \mathbf{R}_J|$, and $F_{IJ}^C(R_{IJ})$ represents the magnitude of conservative force \mathbf{F}_{IJ}^C , which is distance dependent and can be equally replaced by a constant α multiplying a weighting function $\omega_C(R_{IJ})$.

To compute the magnitude of the conservative force $F_{IJ}^C(R_{IJ}) = \alpha \cdot \omega_C(R_{IJ})$, we divide the distance between two molecules into many bins with width of δ . The value of $F_{IJ}^C(R_{IJ})$ is obtained by averaging the result of $\langle \mathbf{F}_{IJ} \cdot \mathbf{e}_{IJ} \rangle$ over all those pairs I and J with intermolecular distance between $R_{IJ} - \delta/2$ and $R_{IJ} + \delta/2$. Figure 5 shows the conservative force $F_{IJ}^C(R_{IJ})$ versus the intermolecular distance R_{IJ} for the cases $N_c = 11, 21$ and 31 at $\rho = 0.4$ and $k_B T = 1.0$. At short distances the RDF of COM rapidly approaches zero, which indicates the improbability of pairs at very short distances. This is the reason why there are no data available at short distances in Fig. 5.

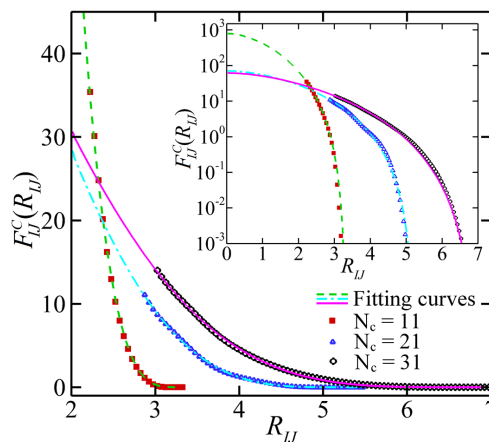


Fig. 5: Conservative force $F_{IJ}^C(R_{IJ})$ versus the intermolecular distance R_{IJ} for the cases $N_c = 11, 21, 31$ at $\rho = 0.4$ and $k_B T = 1.0$.

The computed data obtained from the MD simulations suggest a bell-shaped function $f(R)$ for fitting both conservative and dissipative forces,

$$f(R) = \begin{cases} \Lambda(1 + \chi \frac{R}{R_{cut}})(1 - \frac{R}{R_{cut}})^\chi, & R \leq R_{cut} \\ 0, & R > R_{cut} \end{cases} \quad (17)$$

where Λ and χ are two undetermined coefficients, and R_{cut} is a cutoff radius for fitting the data. In Eq. (17) a weighting function can be defined as $\omega(R) = (1 + \chi \cdot R/R_{cut})(1 - R/R_{cut})^\chi$, which has its maximum value 1.0 at $R = 0$ and smoothly decays to 0 at $R = R_{cut}$. For the conservative force, the cutoff radius R_{cut} is determined by the distance beyond which the pairwise force $F_{IJ}^C(R_{IJ})$ is smaller than $10^{-6} \cdot F_{max}^C$, where F_{max}^C is the maximum value of available data of $F_{IJ}^C(R_{IJ})$. Using the least squares method, the data in Fig. 5 are best fitted with parameter sets (Λ, χ, R_{cut}) , which are given as (795.69, 4.00, 3.32) for $N_c = 11$, (71.09, 3.75, 5.23) for $N_c = 21$, and (61.97, 4.55, 6.97) for $N_c = 31$. These fitting functions in the form of Eq. (17) will be used as the conservative force for DPD models in section 4. A global view of these fitting curves is provided in the inset of Fig. 5.

3.3.2 Non-Conservative forces. With the pairwise approximation, the total fluctuating force $\delta\mathbf{F}_I$ on a cluster I is approximated by $\delta\mathbf{F}_I \approx \sum_{J \neq I} \delta\mathbf{F}_{IJ}$ in which $\delta\mathbf{F}_{IJ}$ is the pairwise fluctuating force defined as,

$$\delta\mathbf{F}_{IJ} = \mathbf{F}_{IJ} - \langle \mathbf{F}_{IJ} \rangle, \quad (18)$$

where \mathbf{F}_{IJ} is the instantaneous force exerted by cluster J on cluster I , and $\langle \mathbf{F}_{IJ} \rangle$ is the ensemble average of \mathbf{F}_{IJ} obtained by Eq. (16).

Generally, the fluctuating force $\delta\mathbf{F}_{IJ}$ is not parallel to the radial direction \mathbf{e}_{IJ} . However, $\delta\mathbf{F}_{IJ}$, on average, is transversely isotropic with respect to \mathbf{e}_{IJ} because the instantaneous pairwise force \mathbf{F}_{IJ} has no preference between directions \perp_1 and \perp_2 , as shown in Fig. 4. Here, when we calculate the magnitude of perpendicular fluctuating force, we do not distinguish between the directions \perp_1 and \perp_2 and decompose $\delta\mathbf{F}_{IJ}$ into two parts

$$\begin{aligned} \delta\mathbf{F}_{IJ} &= (\mathbf{e}_{IJ}\mathbf{e}_{IJ}^T) \cdot \delta\mathbf{F}_{IJ} + (\mathbf{1} - \mathbf{e}_{IJ}\mathbf{e}_{IJ}^T) \cdot \delta\mathbf{F}_{IJ} \\ &= \delta\mathbf{F}_{IJ}^{\parallel} + \delta\mathbf{F}_{IJ}^{\perp}, \end{aligned} \quad (19)$$

where $\delta\mathbf{F}_{IJ}^{\parallel}$ is the component along vector \mathbf{e}_{IJ} and $\delta\mathbf{F}_{IJ}^{\perp}$ the perpendicular part whose modulus is equally distributed on directions \perp_1 and \perp_2 .

The friction tensor between clusters I and J can be calculated from the memory kernel $\boldsymbol{\varphi}_{IJ} = \beta \int_0^{\tau_0} \langle \delta\mathbf{F}_{IJ}(t) \delta\mathbf{F}_{IJ}(0)^T \rangle dt$. The details of the derivation can be found in the works of Lei et al.¹⁵ and Yoshimoto et al.²⁹ We decompose the fluctuating force $\delta\mathbf{F}_{IJ}$ into its radial and perpendicular components. Then, the friction tensor becomes:

$$\begin{aligned} \boldsymbol{\varphi}_{IJ} &= \beta \int_0^{\tau_0} \langle \delta\mathbf{F}_{IJ}(t) \delta\mathbf{F}_{IJ}(0)^T \rangle dt \\ &= \varphi_{\parallel}(R_{IJ}) \mathbf{e}_{IJ}\mathbf{e}_{IJ}^T + \varphi_{\perp}(R_{IJ}) (\mathbf{1} - \mathbf{e}_{IJ}\mathbf{e}_{IJ}^T), \end{aligned} \quad (20)$$

where $\varphi_{\parallel}(R_{IJ})$ and $\varphi_{\perp}(R_{IJ})$ are the radial and perpendicular components of the friction coefficient determined by

$$\begin{aligned} \varphi_{\parallel}(R_{IJ}) &= \beta \int_0^{\tau_0} \langle \delta\mathbf{F}_{IJ}^{\parallel}(t) \cdot \delta\mathbf{F}_{IJ}^{\parallel}(0) \rangle dt \\ &= \gamma_{\parallel} \omega_D^{\parallel}(R_{IJ}) \\ &= \frac{1}{2} \beta [\sigma_{\parallel} \omega_R^{\parallel}(R_{IJ})]^2, \end{aligned} \quad (21)$$

$$\begin{aligned} \varphi_{\perp}(R_{IJ}) &= \frac{1}{2} \beta \int_0^{\tau_0} \langle \delta\mathbf{F}_{IJ}^{\perp}(t) \cdot \delta\mathbf{F}_{IJ}^{\perp}(0) \rangle dt \\ &= \gamma_{\perp} \omega_D^{\perp}(R_{IJ}) \\ &= \frac{1}{2} \beta [\sigma_{\perp} \omega_R^{\perp}(R_{IJ})]^2. \end{aligned} \quad (22)$$

The correlation function $\langle [\delta\mathbf{F}_{IJ}(t)] [\delta\mathbf{F}_{IJ}(0)]^T \rangle$ is time-dependent and the time integrals in Eqs. (21-22) can be continued forever. In practice, Kirkwood⁴³ introduced a cutoff upper limit τ_0 in the time integral. There is no rigorous definition for the specific value of τ_0 except that it should be large enough for the integral to attain the plateau region but short enough not to decay appreciably to zero. The problem of the plateau was further discussed by Suddaby⁴⁴ and Helfand⁴⁵ for a Brownian particle, and Lagarkov and Sergeyev⁴⁶ have proposed to choose as τ_0 the first zero of the FAF, which was justified by Brey and Ordonez⁴⁷, who performed a molecular dynamics simulation and computed the FAF of a massive Brownian particle immersed in a Lennard-Jones fluid. Furthermore, Hijón and collaborators¹³ carried out a constrained dynamics simulation to obtain a plateau of the integral $K(t) = \int_0^{\infty} \langle \delta\mathbf{F}_I(t) \cdot \delta\mathbf{F}_I(0) \rangle dt$, and they found that the plateau in constrained dynamics has similar value as the peak of $K(t)$ in unconstrained dynamics. In the present work we use a cutoff upper limit τ_0 when the integrals in Eqs. (21) and (22) have their first peak to determine the value of $\varphi_{\parallel}(R_{IJ})$ and $\varphi_{\perp}(R_{IJ})$, as shown in Fig. 6.

The radial and perpendicular components of the friction coefficients versus the distance R_{IJ} for the case $N_c = 11$ are p-

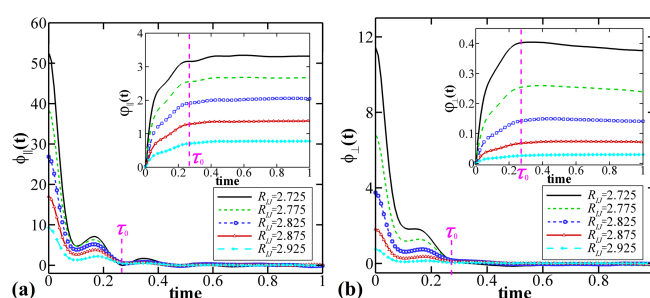


Fig. 6: (a) Time correlations of random force along radial direction $\varphi_{\parallel}(t) = \langle \delta\mathbf{F}_{IJ}^{\parallel}(t) \delta\mathbf{F}_{IJ}^{\parallel}(0) \rangle$ at five intermolecular distances R_{IJ} for the case $N_c = 11$, $\rho = 0.4$ and $k_B T = 1.0$. The insets of (a) and (b) show the value of $\varphi_{\parallel}(t)$ and $\varphi_{\perp}(t)$ given by Eqs. (21-22).

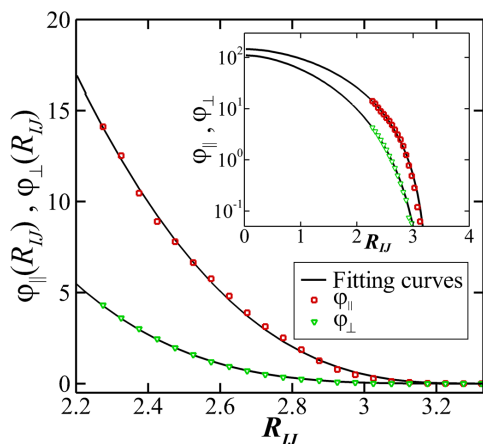


Fig. 7: Radial and perpendicular components of friction coefficients versus the distance R_{IJ} for the case $N_c = 11$. There are no data available for the friction coefficients at $R_{IJ} < 2.2$ because the corresponding $g(r)$ is zero. The fitting parameter set (Λ, χ, R_{cut}) using Eq. (17) for ϕ_{\parallel} is $(146.18, 3.00, 3.32)$, while for ϕ_{\perp} is $(110.76, 3.95, 3.32)$.

resented in Fig. 7. There are no data available for $R_{IJ} < 2.2$ because the corresponding RDF is zero when $R_{IJ} < 2.2$. The parameter sets (Λ, χ, R_{cut}) for fitting the data obtained from MD simulations are listed in table 1, which will be utilized by the DPD models in section 4.

Table 1: Parameters in Eq. (17) for fitting the force fields obtained from MD simulations, also the rotational inertia I_R and cutoff distance R_c (maximum of R_{cut}) for DPD simulations.

N_c	Forces	Λ	χ	R_{cut}	I_R	R_c
11	$\alpha \cdot \omega_C(R)$	795.69	4.00	3.32	6.55	3.32
	$\gamma_{\parallel} \cdot \omega_D^{\parallel}(R)$	146.18	3.00	3.32		
	$\gamma_{\perp} \cdot \omega_D^{\perp}(R)$	110.76	3.95	3.32		
21	$\alpha \cdot \omega_C(R)$	71.09	3.75	5.23	27.51	5.23
	$\gamma_{\parallel} \cdot \omega_D^{\parallel}(R)$	53.58	3.52	5.15		
	$\gamma_{\perp} \cdot \omega_D^{\perp}(R)$	21.86	3.48	5.02		
31	$\alpha \cdot \omega_C(R)$	61.97	4.55	6.97	64.20	6.97
	$\gamma_{\parallel} \cdot \omega_D^{\parallel}(R)$	50.37	4.40	6.93		
	$\gamma_{\perp} \cdot \omega_D^{\perp}(R)$	24.04	4.20	6.70		

4 DPD Models

In this section, we compare four different DPD models and their performances in reproducing the properties of the reference MD system. The first one is the conventional DPD model (DPD), which considers only radial interactions with

empirical weighting functions. The second model is the Mori-Zwanzig DPD model (MZ-DPD), which considers only radial interactions as well, but the MZ-DPD model utilizes the CG force field obtained in section 3. The third is the Mori-Zwanzig Transverse DPD model (MZ-TDPD) considering the interactions in both radial and perpendicular directions. However, the MZ-TDPD excludes the rotational momentum of DPD particles and does not conserve the angular momentum of the system. The last one is the Mori-Zwanzig Full DPD model (MZ-FDPD), which considers the interactions in all the three directions \mathbf{e}_{\parallel} , $\mathbf{e}_{\perp 1}$ and $\mathbf{e}_{\perp 2}$ as well as the rotational motion of DPD particles. It is worth noting that the MZ-FDPD model conserves both the translational and angular momenta of the system. The main differences among these DPD models are summarized in table 2.

Table 2: Description of four DPD models. Here “empirical” force field means empirical weighting functions, while “bottom-up” represents MD-informed CG force field. Symbols \mathbf{V} and $\mathbf{\Omega}$ represent the translational and rotational motions, respectively.

Models	Force Field	Directions of Forces	\mathbf{V}	$\mathbf{\Omega}$
DPD	Empirical	\parallel	Yes	No
MZ-DPD	Bottom-up	\parallel	Yes	No
MZ-TDPD	Bottom-up	$\parallel + \perp_1$	Yes	No
MZ-FDPD	Bottom-up	$\parallel + \perp_1 + \perp_2$	Yes	Yes

4.1 Conventional DPD (DPD)

The time evolution of a DPD particle I is governed by Newton’s equation of motion $d\mathbf{R}_I/dt = \mathbf{V}_I$ and $d\mathbf{P}_I/dt = \mathbf{F}_I = \sum_{J \neq I} (\mathbf{F}_{IJ}^C + \mathbf{F}_{IJ}^D + \mathbf{F}_{IJ}^R)$. The pairwise interaction between DPD particles consists of the conservative force \mathbf{F}_{IJ}^C , dissipative force \mathbf{F}_{IJ}^D and random forces \mathbf{F}_{IJ}^R , which are considered parallel to the radial direction³

$$\mathbf{F}_{IJ}^C = \alpha \cdot \omega_C(R_{IJ}) \mathbf{e}_{IJ}, \quad (23)$$

$$\mathbf{F}_{IJ}^D = -\gamma_{\parallel} \cdot \omega_D^{\parallel}(R_{IJ}) (\mathbf{e}_{IJ} \cdot \mathbf{V}_{IJ}) \mathbf{e}_{IJ}, \quad (24)$$

$$\mathbf{F}_{IJ}^R = \sigma_{\parallel} \cdot \omega_R^{\parallel}(R_{IJ}) \cdot \xi_{IJ}^{\parallel} \Delta t^{-1/2} \mathbf{e}_{IJ}, \quad (25)$$

where R_{IJ} is the distance between particles I and J , \mathbf{e}_{IJ} the unit vector from particle J to I , and $\mathbf{V}_{IJ} = \mathbf{V}_I - \mathbf{V}_J$ the velocity difference. Here, α is repulsive force coefficient, γ_{\parallel} the dissipative coefficient and σ_{\parallel} the strength of random force. ξ_{IJ}^{\parallel} are symmetric Gaussian white noises, which are independent for different pairs of particles and at different times⁴⁸. Also, $\omega_C(R)$, $\omega_D^{\parallel}(R)$ and $\omega_R^{\parallel}(R)$ are the weighting functions of

\mathbf{F}^C , \mathbf{F}^D and \mathbf{F}^R , respectively. The fluctuation-dissipation theorem requires the relationship⁴⁸ $\sigma_{\parallel}^2 = 2\gamma_{\parallel}k_B T$ and $\omega_D^{\parallel}(R) = [\omega_R^{\parallel}(R)]^2$.

A common choice^{3,18,49} for the weighting functions is $\omega_C(R) = 1 - R/R_c$ and $\omega_D^{\parallel}(R) = (1 - R/R_c)^s$ for $R \leq R_c$ and zero for $R > R_c$. With the empirical weighting functions, the parameters α and γ_{\parallel} are optimized to capture the correct pressure and diffusivity of the reference MD system. A parameter set $(\alpha, \gamma_{\parallel}) = (13.5, 32.0)$ with $R_c = 3.4$ and $s = 0.5$ gives pressure $P = 0.194 \pm 0.004$ and diffusivity $D = 0.119 \pm 0.002$ compared to $P = 0.191 \pm 0.006$ and $D = 0.119 \pm 0.002$ of the MD system.

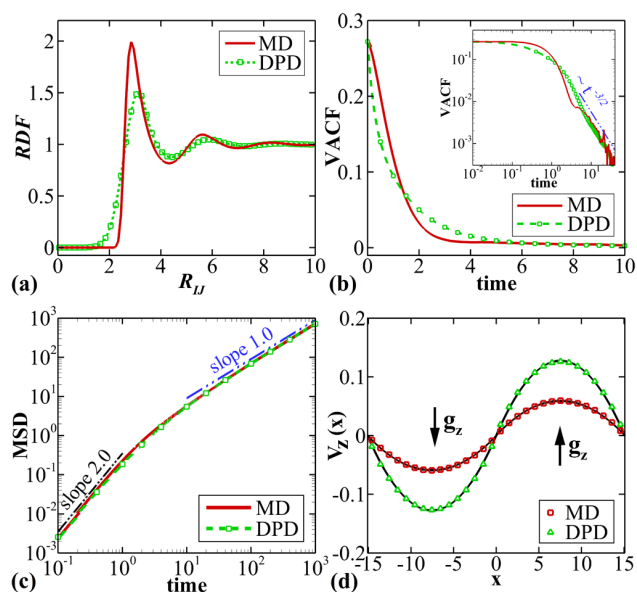


Fig. 8: Performance of the conventional DPD model (DPD) in reproducing the MD system on (a) the radial distribution function (RDF), (b) the velocity autocorrelation function (VACF) and (c) the mean squared displacement (MSD) at $\rho = 0.4$ and $N_c = 11$. (d) Velocity profile for measuring the viscosity with periodic Poiseuille flow.

Figure 8 shows the performance of the conventional DPD model in reproducing the RDF and the VACF of the MD system. The behavior of VACF implicitly includes the dynamical properties of the system. At short timescales particles in the fluid experience the ballistic regime, and the VACF decays exponentially with a characteristic timescale $\tau_p = M/\eta$, where M is the mass of the particle and η is the Stokes viscous drag coefficient. For timescales much larger than τ_p , the VACF shows a long-time tail proportional to $t^{-3/2}$ in the presence of the hydrodynamic memory effects. Correspondingly, the mean squared displacement (MSD) of the particle approaches $(3k_B T/M)t^2$ in the ballistic regime at short timescales, and becomes $6Dt$ at larger times. Moreover, the diffusion constant

D is also related to the VACF via Green-Kubo relations

$$D = \frac{1}{3} \int_0^{\infty} \langle \mathbf{V}(t) \cdot \mathbf{V}(0) \rangle dt. \quad (26)$$

The diffusivity D can be computed by using either the Green-Kubo relation given by Eq. (26) or the Einstein relation $6Dt = \langle |\mathbf{r}(t) - \mathbf{r}(0)|^2 \rangle_{t \rightarrow \infty}$. The two measurements of diffusivity based on MSD and VACF are equal in theory. With the data of MD and DPD simulations, the measurement based on MSD gives 0.120 while the Green-Kubo integral gives 0.119.

To quantitatively compare the mesoscopic system and its underlying microscopic system, the macroscopic properties of the MD and DPD systems are listed in table 3, in which the diffusion constants D are determined by the Green-Kubo integral. The viscosity is computed based on the periodic Poiseuille flow⁵⁰ at low shear rate, as shown in Fig. 8(d) in which the lines are quadratic fit curves for each case. A small body force $g_z = 0.002$ is applied to generate low shear rate flow. To ensure the validity of our measurements a smaller body force $g_z = 0.001$ is also tested and it gives same viscosities.

From table 3 it is obvious that the pressure of the MD system is correctly captured by the DPD model. However, the DPD model has inconsistent RDF compared to that of the reference MD system as shown in Fig. 8(a), which reveals that the local structure and the size of the cluster in MD system are incorrectly reproduced. Moreover, the Stokes-Einstein radius R_{SE} of DPD particle is 2.510 compared to 1.155 of MD system. Furthermore, the VACF of DPD system decays differently from the VACF of MD system, which implies that the viscous forces on the particles are different between the DPD and the MD systems. Table 3 shows that the viscosity of DPD system is approximately half the value of MD system though the diffusivity is correctly reproduced.

4.2 Mori-Zwanzig DPD (MZ-DPD)

The MZ-DPD model has same expressions of forces as the conventional DPD model given by Eqs. (23-25). However, the forces are given by the CG force field obtained in section 3 rather than empirical formulas. The parameters listed in table 1 are utilized to generate the DPD force field. For example, we have $\alpha = 795.69$, $\omega_C(R) = (1 + 4R/3.32)(1 - R/3.32)^4$, $\gamma_{\parallel} = 146.18$ and $\omega_D^{\parallel}(R) = (1 + 3R/3.32)(1 - R/3.32)^3$ corresponding to the MD system $N_c = 11$ at $\rho = 0.4$ and $k_B T = 1.0$.

The comparisons on the RDF and the VACF between the MZ-DPD system and the MD system are made in Fig. 9. We find that the CG force field obtained from MD simulations generates much better results than the empirical force field widely used in the conventional DPD simulations. Without any iteratively optimized parameter, the MZ-DPD model has the same local structure represented by RDF and close VACF

Table 3: Static and dynamic properties for MD and DPD systems at $\rho = 0.4$ and $k_B T = 1.0$, and three degrees of coarse graining $N_c = 11, 21$ and 31 . The symbols P , D , ν , $S_c = \nu/D$ and $R_{SE} = k_B T / (6\pi D \nu \rho)$ represent pressure, diffusivity, kinematic viscosity, Schmidt number and Stokes radius, respectively. The maximum relative statistical error of 32 independent measurements is $\pm 2.3\%$. The errors of different DPD models relative to MD results are displayed in parentheses.

N_c	Models	P (error %)	D (error %)	ν (error %)	S_c (error %)	R_{SE} (error %)
11	MD	0.191	0.119	0.965	8.109	1.155
	DPD	0.194 (+1.6)	0.119 (0)	0.444 (-54.0)	3.731 (-54.0)	2.510 (+117.3)
	MZ-DPD	0.193 (+1.0)	0.138 (+16.0)	0.851 (-11.8)	6.167 (-23.9)	1.129 (-2.2)
	MZ-TDPD	0.193 (+1.0)	0.111 (-6.7)	1.075 (+11.4)	9.685 (+19.4)	1.112 (-3.7)
	MZ-FDPD	0.193 (+1.0)	0.120 (+0.8)	0.954 (-1.1)	7.950 (-2.0)	1.158 (+0.3)
21	MD	0.198	0.061	1.413	23.163	1.539
	MZ-DPD	0.194 (-2.0)	0.083 (+36.1)	1.100 (-22.1)	13.253 (-42.8)	1.453 (-5.6)
	MZ-TDPD	0.194 (-2.0)	0.053 (-13.1)	1.771 (+25.3)	33.415 (+44.3)	1.413 (-8.2)
	MZ-FDPD	0.194 (-2.0)	0.060 (-1.6)	1.457 (+3.1)	24.283 (+4.8)	1.517 (-1.4)
31	MD	0.210	0.040	1.878	46.950	1.765
	MZ-DPD	0.202 (-3.8)	0.059 (+47.5)	1.361 (-27.5)	23.068 (-50.1)	1.652 (-6.4)
	MZ-TDPD	0.202 (-3.8)	0.030 (-25.0)	2.666 (+42.0)	88.867 (+89.3)	1.658 (-6.1)
	MZ-FDPD	0.202 (-3.8)	0.036 (-10.0)	2.087 (+11.1)	57.972 (+23.5)	1.765 (0)

curve as those of the MD system, which means that the MZ-DPD model reproduces better static and dynamical properties than the conventional DPD model.

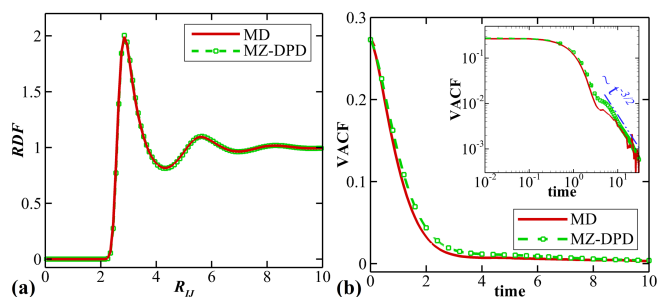


Fig. 9: Performance of the Mori-Zwanzig DPD model (MZ-DPD) in reproducing the MD system on (a) the radial distribution function (RDF) and (b) the velocity autocorrelation function (VACF) at $\rho = 0.4$ and $N_c = 11$.

We note that the MZ-DPD model considers only the radial interaction and neglects the perpendicular forces. The result is an underestimation of the friction between neighbouring particles. Therefore, the MZ-DPD system has smaller viscosity and larger diffusion constant compared to these of the MD system, which can be validated by the data listed in table 3.

4.3 Mori-Zwanzig Transverse DPD (MZ-TDPD)

In addition to the radial forces, the MZ-TDPD model includes the dissipative and random forces in the direction of $\mathbf{e}_{\perp 1}$. The

details of the transverse DPD model can be also found in the work of Junghans and collaborators⁵¹. The equation of motion governing the MZ-TDPD system is given by

$$\begin{aligned}
 \frac{d\mathbf{P}_I}{dt} = & \sum_{J \neq I} \mathbf{F}_{IJ} = \sum_{J \neq I} \alpha \cdot \omega_C(R_{IJ}) \mathbf{e}_{IJ} \\
 & - \sum_{J \neq I} \gamma_{\parallel} \cdot \omega_D^{\parallel}(R_{IJ}) (\mathbf{e}_{IJ} \cdot \mathbf{V}_{IJ}) \mathbf{e}_{IJ} \\
 & - \sum_{J \neq I} \gamma_{\perp} \cdot \omega_D^{\perp}(R_{IJ}) [\mathbf{V}_{IJ} - (\mathbf{e}_{IJ} \cdot \mathbf{V}_{IJ}) \mathbf{e}_{IJ}] \\
 & + \sum_{J \neq I} \sigma_{\parallel} \cdot \omega_R^{\parallel}(R_{IJ}) \cdot \xi_{IJ}^{\parallel} \Delta t^{-1/2} \mathbf{e}_{IJ} \\
 & + \sum_{J \neq I} \sqrt{2} \sigma_{\perp} \cdot \omega_R^{\perp}(R_{IJ}) \cdot \xi_{IJ}^{\perp} \Delta t^{-1/2} \mathbf{e}_{IJ}^{\perp 1}, \quad (27)
 \end{aligned}$$

where $\sigma_{\perp}^2 = 2\gamma_{\perp} k_B T$ and $\omega_D^{\perp}(R) = [\omega_R^{\perp}(R)]^2$. The dissipative and random forces in the direction of \mathbf{e}_{IJ} , as well as those forces in $\mathbf{e}_{IJ}^{\perp 1}$, obey the fluctuation-dissipation theorem to maintain the MZ-TDPD system at constant temperature.

Since the RDF is only determined by the conservative force, the changes of non-conservative forces will not affect the RDF even if the DPD thermostat is replaced by the Nosé-Hoover thermostat we still have the same RDF. Because the MZ-DPD, MZ-TDPD and MZ-FDPD models use the same conservative force, these models have the same RDF as shown in Fig. 9(a), hence only the RDF of the MZ-DPD model is displayed in this paper.

Since the forces between particles in the MZ-TDPD model are not central while the rotational motions of the particles are

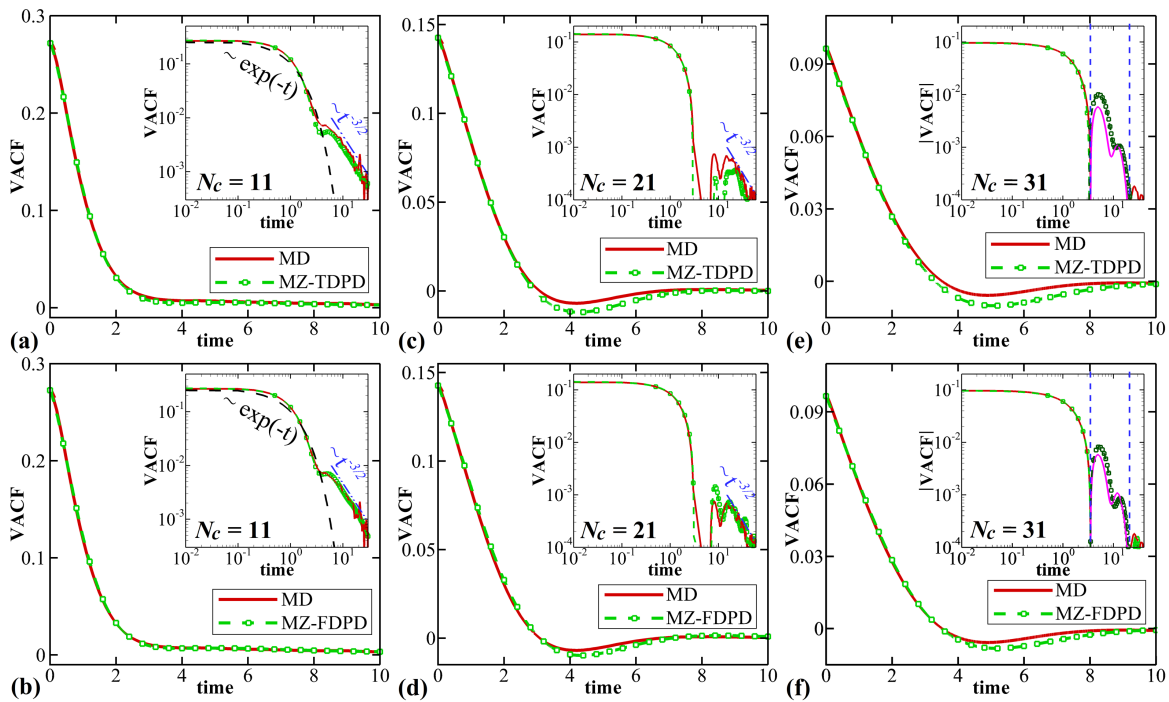


Fig. 10: Performances of Mori-Zwanzig Transverse DPD model (MZ-TDPD) and Mori-Zwanzig Full DPD model (MZ-FDPD) in reproducing the velocity autocorrelation function (VACF) of the MD systems for the cases with (a,b) $N_c = 11$, (c,d) $N_c = 21$ and (e,f) $N_c = 31$ at $\rho = 0.4$. The negative values of the VACF in the insets of (e,f) are displayed between the two vertical dashed lines. The dashed lines show exponential decay ($3k_B T/M \cdot e^{-t}$) in (a,b) and the dash-double dotted lines show algebraic decay. The slopes ($-3/2$) are drawn for reference.

excluded, the angular momentum of the MZ-TDPD system is not conserved⁵¹. By imposing the perpendicular forces in the absence of rotational motions, the friction between neighbouring particles is overestimated by the MZ-TDPD model. Therefore, the viscosity of the MZ-TDPD system is higher than the MD system. As a result, it can be observed in Fig. 10(a) that the MZ-TDPD model yields a VACF below that of the MD system.

4.4 Mori-Zwanzig Full DPD (MZ-FDPD)

The Mori-Zwanzig Full DPD model has the same formulation as the fluid particle model (FPM) proposed by Español⁵², which considers the interactions in all the three directions \mathbf{e}_{\parallel} , $\mathbf{e}_{\perp 1}$ and $\mathbf{e}_{\perp 2}$ shown in Fig. 4, and includes the rotational motions of DPD particles. Compared to the MZ-TDPD model, the MZ-FDPD model also conserves the angular momentum of the system since the particles are allowed to rotate. The time evolutions of the MZ-FDPD particles are governed by^{18,52}

$$\frac{d\mathbf{L}_I}{dt} = \mathbf{T}_I = \sum_{J \neq I} \frac{\mathbf{R}_{IJ}}{2} \times \mathbf{F}_{IJ}, \quad (28)$$

$$\begin{aligned} \frac{d\mathbf{P}_I}{dt} &= \sum_{J \neq I} \mathbf{F}_{IJ} = \sum_{J \neq I} \alpha \cdot \omega_C(R_{IJ}) \mathbf{e}_{IJ} \\ &\quad - \sum_{J \neq I} \gamma_{\parallel} \cdot \omega_D^{\parallel}(R_{IJ}) (\mathbf{e}_{IJ} \cdot \mathbf{V}_{IJ}) \mathbf{e}_{IJ} \\ &\quad - \sum_{J \neq I} \gamma_{\perp} \cdot \omega_D^{\perp}(R_{IJ}) [\mathbf{V}_{IJ} - (\mathbf{e}_{IJ} \cdot \mathbf{V}_{IJ}) \mathbf{e}_{IJ}] \\ &\quad - \sum_{J \neq I} \gamma_{\perp} \cdot \omega_D^{\perp}(R_{IJ}) \left[\frac{\mathbf{R}_{IJ}}{2} \times (\boldsymbol{\Omega}_I + \boldsymbol{\Omega}_J) \right] \\ &\quad + \sum_{J \neq I} \frac{1}{\sqrt{3}} \sigma_{\parallel} \cdot \omega_R^{\parallel}(R_{IJ}) \Delta t^{-1/2} \cdot \text{tr}[d\mathbf{W}_{IJ}] \mathbf{e}_{IJ} \\ &\quad + \sum_{J \neq I} \sqrt{2} \sigma_{\perp} \cdot \omega_R^{\perp}(R_{IJ}) \Delta t^{-1/2} \cdot d\mathbf{W}_{IJ}^A \cdot \mathbf{e}_{IJ}, \quad (29) \end{aligned}$$

where $\boldsymbol{\Omega}_I$ is the angular velocity of particle I , \mathbf{T}_I is the torque and $\mathbf{L}_I = I_{R_I} \boldsymbol{\Omega}_I$ the angular momentum. The magnitudes of the rotational inertia for $N_c = 11, 21$ and 31 are listed in table 1. Also, $d\mathbf{W}_{IJ}$ is a matrix of independent Wiener increments and $d\mathbf{W}_{IJ}^A = \frac{1}{2}(d\mathbf{W}_{IJ}^{\mu\nu} - d\mathbf{W}_{IJ}^{\nu\mu})$ is an antisymmetric noise matrix.

After including the rotational motion of the particles, the MZ-FDPD model has better performance than both the MZ-TDPD and the MZ-DPD models. Fig. 10(b) shows the comparison of the VACF between MD and MZ-FDPD systems for

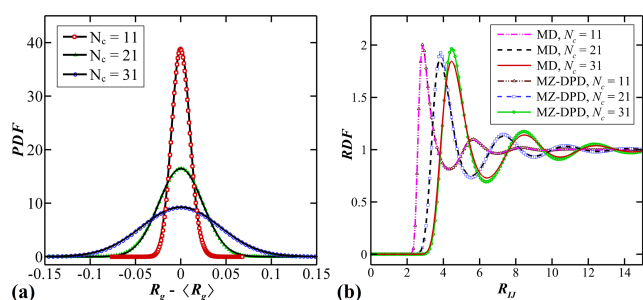


Fig. 11: (a) Probability density functions (PDF) of the gyration radius and (b) radial distribution functions (RDF) for MD clusters of the cases $N_c = 11, 21, 31$ at $\rho = 0.4$ and $k_B T = 1.0$. Mean gyration radius $\langle R_g \rangle = 0.945, 1.402$ and 1.763 for $N_c = 11, 21$ and 31 , respectively.

the case $N_c = 11$. It can be seen that both the short time behavior with an exponentially decay and the long-time tail proportional to $t^{-3/2}$ are correctly reproduced by the MZ-FDPD model, which reveals that the transport properties of the MZ-FDPD system are consistent with those of the MD system.

For these star polymers with long arms, each cluster is surrounded by its near neighbors in a cage-like structure and as soon as the cluster moves it is likely to hit the wall of the cage and will be pushed back. As a result, the VACF becomes negative after a few collisions for the cases $N_c = 21$ and $N_c = 31$ under this backscattering effect, as shown in Fig. 10(c-f). Figure 11(a) shows the PDF of the gyration radius of the MD clusters for cases $N_c = 11, 21$ and 31 , which reveals that the clusters are elastic with variable radius. When we use identically sized DPD particles to represent these clusters, the variations of particle size are neglected, which results in larger peak values in RDF as shown in Fig. 11(b). Although the MD-informed DPD models are able to capture this backscattering effect, Fig. 10(f) shows that the negative part of VACF is not accurately reproduced because the effects induced by the variations of the cluster size are not considered in the DPD model.

Figure 12 displays the Green-Kubo integral of the VACF using Eq. (26) for the cases $N_c = 11, 21$ and 31 . For all the cases, the magnitude of the plateau of $D(t)$ determines the diffusion constant of each system. The dashed horizontal line denotes the diffusivity obtained based on MSD of the MD system. It explicitly shows that the MZ-DPD generates higher diffusivity because of the underestimation of the friction between neighboring particles, while the MZ-TDPD has lower diffusivity resulting from the overestimation of the friction.

Our results here show that the MZ-FDPD model has the best performance in accurately reproducing the MD system. It works well for the star polymer with short arms such as $N_c = 11$ and 21 . However, as the length of arm increases, the relative error becomes -10.0% on the diffusivity and $+11.1\%$

on the viscosity for the case with $N_c = 31$. The reason appears to be that we ignored the many-body correlations between different pairs during the coarse-graining procedure, however, such correlations become significant for polymers with long arms.

5 Summary and Discussion

Based on microscopic simulations of star polymer melts in a canonical ensemble, we extracted mesoscopic force fields for coarse-grained models by mapping the microscopic system to a coarse-grained/mesoscopic system via the Mori-Zwanzig projection. Two main assumptions, Markovian approximation and pairwise approximation, have been used to implement the coarse-graining process. Based on the Mori-Zwanzig formulation, the fast degrees of freedom in the microscopic system are eliminated and their effects can be approximated by a stochastic dynamics under the effects of dissipative and fluctuating interactions, which is consistent with the framework of dissipative particle dynamics (DPD). Therefore, we consider the DPD model to be the effective dynamics resulting from a projection of the underlying atomistic dynamics.

By grouping many bonded atoms of the molecular dynamics (MD) system into a single cluster, we evaluated both the conservative and non-conservative interactions between neighboring clusters and constructed the coarse-grained (CG) force field governing the motion of CG particles. Since the MD clusters consist of discrete particles, the interactions between these finite-size clusters are not parallel to the radial direction. As a result, the CG force field obtained from MD simulations has both radial and perpendicular components. Moreover, the rotational motion of the cluster could be another CG variable to be considered because it carries the same kinetic energy as the translational motion. However, the conventional DPD model accounts for radial interactions only and ignores the perpendicular forces obtained from MD simulations. Obviously, we need other DPD models to include the perpendicular interactions as well as the rotational motions of particles. To this end, we employed four DPD models to consider different microscopic information and compared their performances in reproducing the MD system.

The first DPD model we tested is the conventional DPD model (DPD), which includes only radial interactions and has empirical weighting functions with adjustable parameters. The parameters of the DPD model are optimized to capture the correct values of pressure and diffusivity. With the empirical formulae, the DPD model incorrectly generates the radial distribution function (RDF), the viscosity and the Schmidt number.

The second one is the Mori-Zwanzig DPD model (MZ-DPD), which also considers only the radial interactions. But the MZ-DPD model utilizes the MZ-guided CG force fields

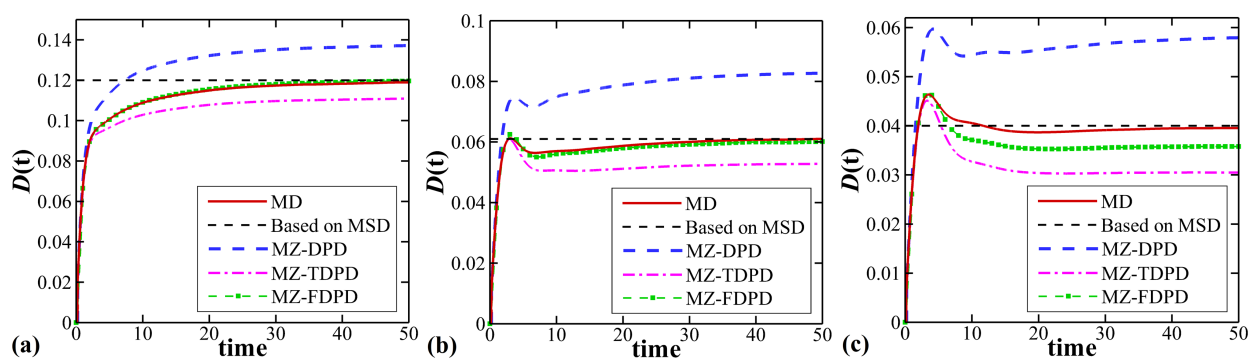


Fig. 12: The time integral of VACF defined by $D(t) = \frac{1}{3} \int_0^t \langle \mathbf{V}(\tau) \mathbf{V}(0) \rangle d\tau$ with different models for star polymers (a) $N_c = 11$, (b) $N_c = 21$ and (c) $N_c = 31$ at $\rho = 0.4$.

obtained from the MD simulations rather than empirical formulae. We would like to emphasize that, without any iteratively optimized parameters, the MZ-DPD model generates the same local structure represented by the RDF and close velocity autocorrelation function as those of its underlying MD system. However, since perpendicular forces are neglected in this model, the result is an underestimation of the friction between neighbouring particles. Therefore, the MZ-DPD systems have smaller viscosity and larger diffusion constant compared to their MD systems.

The third model is the Mori-Zwanzig Transverse DPD model (MZ-TDPD). In addition to the radial forces, the MZ-TDPD model includes the dissipative and random forces in the transverse direction. By imposing the perpendicular forces in the absence of rotational motions, the friction between neighbouring particles is overestimated in the MZ-TDPD model. Thus, the MZ-TDPD system has larger viscosity and smaller diffusivity than its MD system. It is worth noting that the angular momentum of the MZ-TDPD model is not conserved because the forces between particles are not central while the rotational motion of the particles is not accounted for.

The last DPD model we employed is the Mori-Zwanzig Full DPD model (MZ-FDPD). It considers the interactions in all the three directions and also the rotational motions of the particles. After the rotational motion of the particles is taken into account, the MZ-FDPD model has the best performance in reproducing the MD system. Both the short time behavior distinguished by an exponentially decay and the long-time tail proportional to $t^{-3/2}$ in the VACF are correctly reproduced by the MZ-FDPD model, which reveals that the transport properties of the MZ-FDPD system are consistent with those of the MD system.

Compared to the CG procedure reported by Hijón and collaborators¹³, who also studied the polymer melts, we used the FENE bonds rather than harmonic springs to minimise bond crossings in the MD systems. Moreover, we considered more

microscopic information in our DPD models, especially the rotational motion. Therefore, the performance of the MD-informed DPD model has been improved.

It is worthy noting that the rotational motion does not affect the static properties, and hence the MZ-DPD, MZ-TDPD and MZ-FDPD models result in the same static properties, e.g. pressure and RDF. However, the rotational motion does affect the time correlations and the dynamic properties, which is verified by the data listed in Table 3 and Fig. 12. This conclusion is obtained in the short nonentangled polymer systems. Limited by the Markovian approximation, we do not study dense polymer melts or high volume fractions. It is not clear that if the rotational motion is still important for the dynamic properties in coarse-graining of dense polymer melts. Nevertheless, without the rotational dynamics together with transverse interactions, the conservation of the angular momentum is definitely violated.

The present work provides a direct relationship between the mesoscopic system and its underlying microscopic system. It also proposes a general methodology to construct coarse-grained force fields from the information provided by atomistic simulations. This strategy of coarse-graining is not relevant to any specific system and can be employed for other systems in which the clusters can be faithfully defined as CG particles. With a MD system of polymer melts, we demonstrated that a coarse-grained model without any iteratively optimized parameter can accurately reproduce the entire VACF as well as the correct RDF of its underlying microscopic system.

We note that the approximations introduced in section 2 are applied to make the Mori-Zwanzig formulation practical. Therefore, the performance of the coarse-graining method relies on whether those approximations are valid for specific systems. Although we have shown that the MZ-FDPD model has excellent performance in reproducing the MD system of polymers with short arms, the errors on macroscopic properties between the MD and MZ-FDPD systems becomes large

($\sim 10\%$ error at $N_c = 31$) for the polymer with long arms. The reason appears to be that we assumed that the non-bonded interactions between neighboring clusters in the microscopic system are explicitly pairwise decomposable and ignored the many-body correlations between different pairs. However, for the polymer with long arms, polymer entanglements yield strong many-body correlations and such approximation will work less effectively. In future work we plan to reformulate the DPD model to also consider the many-body correlations for those polymers with long arms.

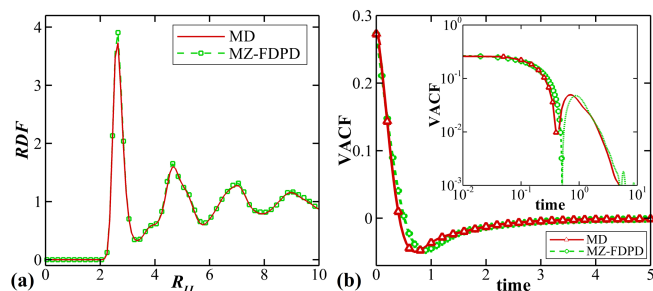


Fig. 13: For $\rho = 0.8$ and $N_c = 11$, the performance of the Mori-Zwanzig Full DPD model (MZ-FDPD) in reproducing its underlying MD system on (a) the radial distribution function (RDF) and (b) the velocity autocorrelation function (VACF). The negative values of the VACF in the inset of (b) are displayed by lines without symbols.

Furthermore, we employed the Markovian approximation to compute the memory kernel of the dissipative force. However, we have already noted that the validity of the Markovian approximation is questionable for polymer melts at high density (see Fig. 2(b)), in which the typical time scales of the momenta and the fluctuating forces are not fully separable. Since the Markovian approximation does not affect the static properties, the MZ-guided DPD model can still reproduce the correct static properties, e.g. pressure and RDF, even for polymers at high densities, as shown in Fig. 13(a). However, for the dynamic response, the failure of the Markovian approximation yields incorrect time correlations and hence wrong dynamic properties. Figure 13(b) displays the performance of the MZ-FDPD model in reproducing the VACF of its underlying MD system at $\rho = 0.8$. The results show that the characteristic timescale of exponential decay in VACF of the MZ-FDPD model differs from that of the MD system, which reveals that errors in dynamic properties induced by the Markovian approximation become significant. In future work we plan to correct this error by preserving the memory effects of interactions rather than involving a Markovian approximation.

Acknowledgements

The authors acknowledge Dr. Huan Lei, Dr. Mingge Deng and Dr. Changho Kim for helpful discussions, and Dr. Yu-Hang Tang for computational support. This work was supported by the new DOE Center on Mathematics for Mesoscopic Modeling of Materials (CM4). Computations were performed at the IBM BG/P with computer time provided by an INCITE grant.

References

- Z. G. Mills, W. B. Mao and A. Alexeev, *Trends Biotechnol.*, 2013, **31**, 426–434.
- J. Buchholz, W. Paul, F. Varnik and K. Binder, *J. Chem. Phys.*, 2002, **117**, 7364–7372.
- R. D. Groot and P. B. Warren, *J. Chem. Phys.*, 1997, **107**, 4423–4435.
- M. G. Saunders and G. A. Voth, *Annu. Rev. Biophys.*, 2013, **42**, 73–93.
- E. Brini, E. A. Algaer, P. Ganguly, C. L. Li, F. Rodriguez-Roperio and N. F. A. van der Vegt, *Soft Matter*, 2013, **9**, 2108–2119.
- M. A. Katsoulakis and P. Plecháč, *J. Chem. Phys.*, 2013, **139**, 074115.
- P. Español and I. Zúñiga, *Phys. Chem. Chem. Phys.*, 2011, **13**, 10538–10545.
- A. J. Clark, J. McCarty, I. Y. Lyubimov and M. G. Guenza, *Phys. Rev. Lett.*, 2012, **109**, 168301.
- H. Mori, *Prog. Theor. Phys.*, 1965, **33**, 423–455.
- R. Zwanzig, *Nonequilibrium Statistical Mechanics*, Oxford University Press, New York, 2001.
- R. L. C. Akkermans and W. J. Briels, *J. Chem. Phys.*, 2000, **113**, 6409–6422.
- T. Kinjo and S. A. Hyodo, *Phys. Rev. E*, 2007, **75**, 051109.
- C. Hijón, P. Español, E. Vanden-Eijnden and R. Delgado-Buscalioni, *Faraday Discuss.*, 2010, **144**, 301–322.
- G. J. Phillies, in *Projection Operators and the Mori-Zwanzig Formalism*, Springer New York, 2000, ch. 32, pp. 347–364.
- H. Lei, B. Caswell and G. E. Karniadakis, *Phys. Rev. E*, 2010, **81**, 026704.
- P. Hoogerbrugge and J. Koelman, *Europhys. Lett.*, 1992, **19**, 155–160.
- Z. L. Li and E. E. Dormidontova, *Soft Matter*, 2011, **7**, 4179–4188.
- W. X. Pan, B. Caswell and G. E. Karniadakis, *Langmuir*, 2010, **26**, 133–142.
- Z. Li, G. H. Hu, Z. L. Wang, Y. B. Ma and Z. W. Zhou, *Phys. Fluids*, 2013, **25**, 072103.
- X. J. Li, P. M. Vlahovska and G. E. Karniadakis, *Soft Matter*, 2013, **9**, 28–37.
- A. P. Lyubartsev and A. Laaksonen, *Phys. Rev. E*, 1995, **52**, 3730–3737.
- D. Reith, M. Putz and F. Muller-Plathe, *J. Comput. Chem.*, 2003, **24**, 1624–1636.
- F. Ercolessi and J. B. Adams, *Europhys. Lett.*, 1994, **26**, 583–588.
- M. S. Shell, *J. Chem. Phys.*, 2008, **129**, 144108.
- S. Izvekov and G. A. Voth, *J. Phys. Chem. B*, 2005, **109**, 2469–2473.
- W. G. Noid, *J. Chem. Phys.*, 2013, **139**, 090901.
- S. Izvekov and G. A. Voth, *J. Chem. Phys.*, 2006, **125**, 151101.
- S. Trément, B. Schnell, L. Petitjean, M. Couty and B. Rousseau, *J. Chem. Phys.*, 2014, **140**, 134113.
- Y. Yoshimoto, I. Kinefuchi, T. Mima, A. Fukushima, T. Tokumasu and S. Takagi, *Phys. Rev. E*, 2013, **88**, 043305.
- Y. T. Wang, W. G. Noid, P. Liu and G. A. Voth, *Phys. Chem. Chem. Phys.*, 2009, **11**, 2002–2015.
- P. Español, *Phys. Rev. E*, 1996, **53**, 1572–1578.
- J. F. Rudzinski and W. G. Noid, *J. Phys. Chem. B*, 2012, **116**, 8621–8635.

-
- 33 A. Jusufi, M. Watzlawek and H. Lowen, *Macromolecules*, 1999, **32**, 4470–4473.
- 34 Q. Zhou and R. G. Larson, *Macromolecules*, 2007, **40**, 3443–3449.
- 35 J. D. Weeks, D. Chandler and H. C. Andersen, *J. Chem. Phys.*, 1971, **54**, 5237–5247.
- 36 K. Kremer and G. S. Grest, *J. Chem. Phys.*, 1990, **92**, 5057–5086.
- 37 J. G. H. Cifre, S. Hess and M. Kroger, *Macromol. Theory Simul.*, 2004, **13**, 748–753.
- 38 M. Cheon, I. Chang, J. Koplik and J. R. Banavar, *Europhys. Lett.*, 2002, **58**, 215–221.
- 39 M. Kroger and S. Hess, *Phys. Rev. Lett.*, 2000, **85**, 1128–1131.
- 40 S. Nosé, *J. Chem. Phys.*, 1984, **81**, 511–519.
- 41 W. G. Hoover, *Phys. Rev. A*, 1985, **31**, 1695–1697.
- 42 E. Saldivar-Guerra and E. Vivaldo-Lima, *Handbook of Polymer Synthesis, Characterization, and Processing*, John Wiley and Sons, Hoboken, 2013.
- 43 J. G. Kirkwood, *J. Chem. Phys.*, 1946, **14**, 180–201.
- 44 A. Suddaby and P. Gray, *Proc. Phys. Soc.*, 1960, **75**, 109–118.
- 45 E. Helfand, *Phys. Fluids*, 1961, **4**, 681–691.
- 46 A. N. Lagarkov and V. M. Sergeev, *Sov. Phys. Usp.*, 1978, **21**, 566–588.
- 47 J. J. Brey and J. G. Ordóñez, *J. Chem. Phys.*, 1982, **76**, 3260–3263.
- 48 P. Español and P. Warren, *Europhys. Lett.*, 1995, **30**, 191–196.
- 49 X. J. Fan, N. Phan-Thien, S. Chen, X. H. Wu and T. Y. Ng, *Phys. Fluids*, 2006, **18**, 063102.
- 50 J. A. Backer, C. P. Lowe, H. C. J. Hoefsloot and P. D. Iedema, *J. Chem. Phys.*, 2005, **122**, 154503.
- 51 C. Junghans, M. Praprotnik and K. Kremer, *Soft Matter*, 2008, **4**, 156–161.
- 52 P. Español, *Phys. Rev. E*, 1998, **57**, 2930–2948.